Ocean Engineering 344 (2026) 123610

Contents lists available at ScienceDirect

Ocean Engineering

journal homepage: www.elsevier.com/locate/oceaneng

Research paper

Non-causal economic model predictive control for ocean wave energy maximisation based on wave-to-wire model

Teng Gao [a], Yao Zhang [b,*], Tahsin Tezdogan [a]

[a] School of Engineering, University of Southampton, Southampton, SO17 1BJ, United Kingdom
[b] Department of Mechanical Engineering, University College London, London, WC1E 7JE, United Kingdom

ARTICLE INFO

Keywords:
Economic model predictive control (EMPC)
Wave-to-wire
Wave energy conversion

ABSTRACT

This paper proposes a non-causal economic model predictive control (EMPC) strategy based on wave prediction and integrated within the wave-to-wire model, aiming to improve the energy conversion efficiency of wave energy converters (WECs) and ensure safe operation under diverse sea states. Extending conventional EMPC approaches that primarily consider mechanical-side dynamics, this study integrates both mechanical and electrical subsystems within a unified wave-to-wire model and imposes a PTO control-input rate constraint to allow capturing the complete energy conversion path while ensuring electrical feasibility. The proposed non-causal EMPC guarantees recursive feasibility and satisfaction of safety constraints. It directly optimises an economic performance criterion that maximises energy extraction and minimises operational costs. The wave-to-wire model enables accurate evaluation of output energy through electrical variables such as generator current and voltage, thereby enhancing conversion efficiency. Taking a point absorber as a case study, simulation results demonstrate that the proposed framework achieves substantial improvements in energy production compared with conventional tracking-based MPC formulations. These findings confirm its effectiveness and highlight its potential for practical deployment in wave energy conversion control.

1. Introduction

As fossil fuel resources become increasingly depleted in the coming decades, the development of clean energy has become a global goal. As a form of ocean renewable energy, wave energy offers high energy density, strong predictability, and a reliable supply. Its theoretical annual power generation capacity could reach approximately 32,000 kWh. Wave energy resources are primarily distributed in mid- and high-latitude oceans, such as the west coast of North America, southern Australia, the British Isles, the west coast of Europe, southern Chile, and New Zealand (Gao et al., 2025). The total potential in coastal areas worldwide is estimated to exceed 2 TW (Gunn and Stock-Williams, 2012). Compared to wind and solar energy, wave energy offers significant advantages in energy density and stability (Falnes and Kurniawan, 2020). However, the commercialisation of wave energy remains immature, primarily due to low energy conversion efficiency and a high risk of structural damage under certain sea conditions (Drew et al., 2009).

Reports on the utilisation of wave energy can be traced back to the 18th century, with Salter's research laying the foundation for large-scale wave power generation (Salter, 1974). However, achieving optimal energy conversion requires large-scale devices, which pose significant design challenges. Over the past few decades, people have conducted extensive research on the control strategies of wave energy converters (WECs). WECs such as point absorbers, oscillating water columns and attenuators have been studied and developed (Manan Jariwala et al., 2025). Wave prediction methods such as the extended Kalman filter (EKF), artificial neural networks, and deterministic sea wave prediction (DSWP) all introduce certain prediction errors. Based on the simple control method (SCM), practical prediction techniques have been improved and applied to wave observations, enabling near-accurate and simultaneous prediction of the hydrodynamic forces acting on a WEC. A common form of this type of system directly utilises the relative motion between the coil and the permanent magnet to generate electricity. By using analytical background and numerical methods to derive the optimal control force parameters, the power generation of multiple PA-WEC arrays can be maximised (Murai et al., 2021). However, the frequency response of the point absorber WEC is narrow and its performance is unsatisfactory under realistic ocean conditions unless its motion is actively controlled (Hals et al., 2011).

Model predictive control (MPC) is widely used in wave energy systems to handle strong dynamics and complex constraints (Zhang et al., 2020). However, many conventional MPC strategies do not consider

* Corresponding author.
E-mail addresses: Teng.Gao@soton.ac.uk (T. Gao), yao.zhang@ucl.ac.uk (Y. Zhang), T.Tezdogan@soton.ac.uk (T. Tezdogan).

https://doi.org/10.1016/j.oceaneng.2025.123610
Received 19 September 2025; Received in revised form 5 November 2025; Accepted 16 November 2025
Available online 29 November 2025

terminal stability constraints or disturbance feedback mechanisms. In this study, conventional MPC refers to the standard linear model predictive control framework that solves a finite-horizon quadratic program (QP) based on measurable mechanical states. It typically employs open-loop prediction and does not explicitly include disturbance feedback or terminal constraints. This formulation is consistent with widely adopted industrial MPC deployments. Their control structures primarily rely on open-loop predictions and lack the ability to handle disturbances and uncertainties in closed-loop systems (Gao et al., 2025). Although traditional tube-based model predictive control (TMPC) is robust to disturbances, it can suffer from steady-state errors in the presence of persistent disturbances (Wijaya et al., 2025). Robust model predictive control (RMPC) ensures recursive feasibility for all disturbances within a prescribed bounded uncertainty set (Zhang et al., 2023). A min-max strategy is employed to evaluate the worst-case cost function (Evans et al., 2014), or a pipeline-based approach is employed to parameterise a partially separable feedback control law (Lasheen et al., 2017) (Garcia-Violini and Ringwood, 2021). Non-causal MPC explicitly incorporates short-term wave forecasting into optimisation, improving energy recovery while maintaining feasibility and constraint satisfaction (Zhan et al., 2019b). Coupling data-driven LSTM wave force prediction with MPC has achieved real-time non-causal control under irregular sea conditions and completed physical experimental verification (Zhang et al., 2024a). Explicit non-causal MPC for online computability reduces the solution burden and facilitates embedded implementation (Gao et al., 2025). Tube-based RMPC for WEC uses set contraction to ensure recursive feasibility and constraint satisfaction under bounded uncertainty (Zhang and Li, 2022). Engineering applications have demonstrated that tube-based RMPC achieves an effective trade-off between performance and conservatism in inertial WECs (Schiavon et al., 2021). Learning-enhanced robust MPC incorporates data-driven uncertainty modelling into an ensemble contraction or cost-shaping framework to improve tolerance to modelling biases and wave prediction errors (Zhang et al., 2024b). There is a conflict between maximising energy capture and ensuring the range of sea conditions under which the system operates safely. This trade-off is difficult to achieve and can reduce the operating range and energy conversion efficiency. The economic feedback MPC control law includes offline design of state feedback gains to maximise the operating range, and online calculation to maximise the captured energy (Zhan et al., 2019a) and optimise the energy conversion efficiency of the WEC.

Models based solely on hydrodynamics struggle to fully evaluate the performance of WECs because they often ignore or oversimplify the role of the PTO system. To this end, researchers have proposed a wave-to-wire framework to uniformly model all stages of the conversion from waves to the grid, while considering the necessary components, dynamic characteristics, and constraints (Penalba and Ringwood, 2016). Existing studies have developed wave-to-wire models for various WECs, including overflow-type (Igic et al., 2011), oscillating water columns (OWCs) (Amundarain et al., 2010), and hydraulic point absorption devices (Josset et al., 2007). Compared with fluid dynamic control that only focuses on maximum energy absorption, the wave-to-wire framework can achieve a more comprehensive trade-off between energy capture efficiency and electrical constraints.

The control problem of a WEC can be viewed as a constrained non-causal energy maximisation (EM) control problem, whose optimal solution depends on future wave information (Zhang and Li, 2019) and whose actual operation is subject to constraints on device motion and actuator capacity. This problem is typically addressed using optimal control strategies to approximate the non-causal optimal solution. In recent years, economic model predictive control (EMPC), originating from the field of process control, has been gradually applied to wave energy research and proposed as an optimisation framework for directly solving energy maximisation problems (Müller and Grüne, 2016). Influenced by the concept of EMPC, several MPC-based WEC control methods have been proposed, among which (Zhan et al., 2019a) introduced an economic feedback model predictive control (EMPC) framework for WEC systems, successfully demonstrating the feasibility of this approach for wave energy conversion. Their formulation primarily focused on the dynamics of the mechanical side. In contrast, this study extends the EMPC concept to a complete wave-to-wire model, integrating mechanical and electrical subsystems with non-causal wave prediction and robust constraint handling. This integrated architecture allows the controller to simultaneously consider electrical dynamics and energy transfer efficiency, thereby providing a more realistic representation of the overall energy conversion process while maintaining recursive feasibility and constraint satisfaction. A hard constraint on the variation rate of PTO force ensures electrical feasibility during the optimisation process.

Most conventional WEC MPC methods adopt an open-loop approach, which has two major limitations in engineering applications. First, they lack recursive feasibility guarantees. The feasible solution of the MPC depends on the current system state, the predicted wave conditions, and the constraints. If all conditions are not met, the optimisation problem becomes unsolvable, and the constraints must be sacrificed to obtain a feasible input. Second, there is an inherent conflict between the objective function's energy capture and safe operating range. Improving energy capture efficiency requires greater float oscillation, but this significantly increases the risk of violating safety constraints and encountering infeasible solutions (Zhan et al., 2019a). Open-loop MPC struggles to find the optimal balance between these two objectives within a single objective function, resulting in a limited operating range and reduced energy conversion efficiency. Therefore, this study aims to develop a non-causal EMPC framework based on a wave-to-wire model for complex WECs to achieve both energy optimisation and safe operation. This framework incorporates fluid dynamics developed from linear wave theory and power take-off (PTO) dynamics on the mechanical side. On the electrical side, the motor and its energy calculation module are considered. Because the actual motion range of the motor is relatively small, the application of linear fluid dynamics to describe the interaction between waves and floating bodies is both reasonable and sufficient.

The main novelties and contributions of this paper are as follows:

1. The proposed non-causal EMPC algorithm does not rely on the traditional quadratic cost of trajectory tracking, but instead directly constructs an economic performance indicator. It organically integrates the mechanical and electrical aspects to create a wave-to-wire framework that goes beyond mechanical energy capture. This is the first application of non-causal EMPC based on the wave-to-wire model in WEC control.
2. Given that WEC control is a non-causal control problem, this paper designs an autoregressive model for wave prediction to maximise energy.
3. Based on a wave-to-wire model, the PTO force-rate (the rate of change of the control input, $\dot{u}$ in continuous time or Δu in discrete time) hard constraint is physically coupled with the voltage/current limits and incorporated into the optimisation. This ensures electrical feasibility during the solution phase and links economic objectives with feasibility.
4. The proposed framework guarantees recursive feasibility and strict satisfaction of state and input constraints throughout operation.
5. Real wave data from the coast of Cornwall, UK (Zhang et al., 2019) (Li and Belmont, 2014) are used to verify the effectiveness of EMPC in wave energy-driven control.
6. The control algorithm flow of this paper is shown in the Algorithm 3.

This paper is organised as follows: Section II presents the mathematical modelling of the WEC dynamic system. Section III analyses the structural design of the non-causal EMPC. Section IV presents the simulation results and analysis. Section V provides an overall conclusion of this paper.

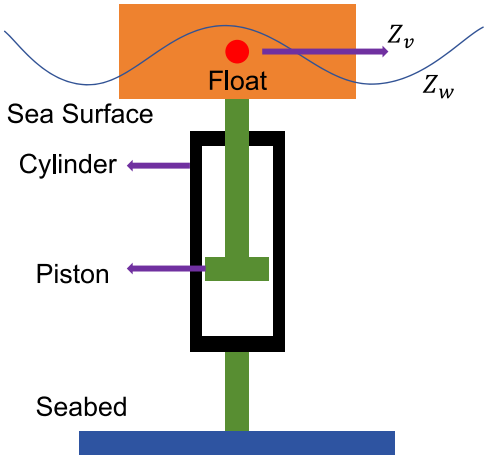

Fig. 1. Schematic diagram of point absorber.

2. Mathematical modelling of WEC dynamic system

This section introduces the dynamic model of a single-point absorber. In Section 2.1, a wave-to-wire model of WECs is established. In Section 2.2, the hydrodynamic model is transformed into a state-space model to design the controller, which introduces modelling uncertainty. Section 2.3 describes how to unify the energy maximisation objective and physical constraints of the WEC into an optimisation problem for a non-causal MPC.

2.1. Wave-to-wire model of WECs

Fig. 1 illustrates a representative hydraulic power take-off (PTO) configuration, in which a hydraulic cylinder is mounted vertically beneath a float and anchored to the seabed. A detailed description of this design can be found in Weiss et al. (2012). The sea surface elevation is denoted as z_w, while z_v represents the vertical position of the float midpoint. The present study focuses primarily on realistic deep-water sea conditions, and shallow-water effects are not considered. To establish a wave-to-wire model from incident wave to electrical energy output, an electrical conversion unit must be introduced following the mechanical-hydraulic subsystem. Specifically, the mechanical work of the hydraulic PTO is converted into electrical energy by the linear electric motor (LEM), and thus the dynamic characteristics of the motor must be incorporated into the overall modelling framework. To this end, this study uses an equivalent circuit model to represent the LEM, an approach that has been widely verified in renewable energy research (Wilson et al., 2018). The corresponding circuit model is illustrated in Fig. 2. R_s and L_s denote the stator resistance and inductance, respectively, while v_{abc} represents the three-phase terminal voltages with respect to the neutral point. The dynamic characteristics of the LEM equivalent circuit can be expressed in the dq reference frame as:

$$\begin{aligned} v_d &= R_s i_d + L_d \frac{di_d}{dt} - \omega_e L_q i_q, \\ v_q &= R_s i_q + L_q \frac{di_q}{dt} + \omega_e L_d i_d + \omega_e \psi_f \end{aligned} \tag{1}$$

where v_{dq}, i_{dq}, and L_{dq} denote the terminal voltage, current, and inductance in the dq frame, respectively; ω_e is the electrical velocity of the LEM, and ψ_f is the field magnetic flux. Considering that the motion of the translator follows the heave motion of the WEC, the linear motion of the device can be converted into an equivalent rotational motion for further calculations by $\omega_e = \frac{2\dot{x}}{r_{\text{eq}} n_p}$. Here, r_{eq} is the equivalent radius related to the permanent magnet design parameter (pole pitch), and n_p is the number of pole pairs of the LEM. The force generated by the LEM can be computed as:

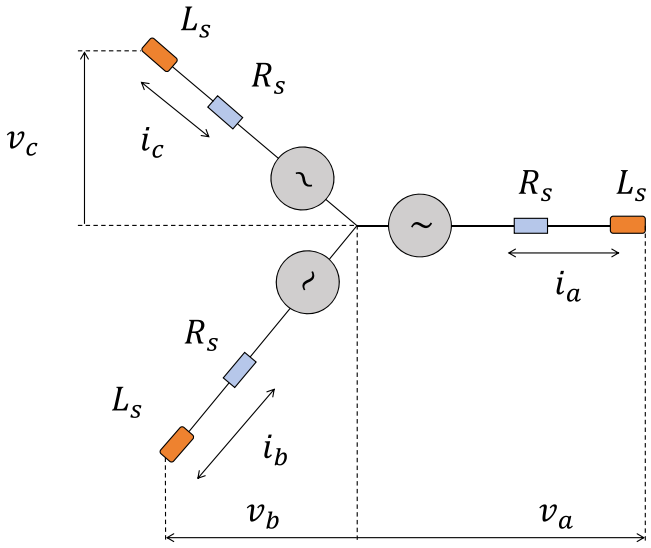

Fig. 2. Linear electrical machine equivalent circuit model.

$$F_{\text{PTO}} = -\frac{n_p}{r_{\text{eq}}} \sqrt{\frac{3}{2}} \left(i_q \psi_f + (L_d - L_q) i_d i_q \right) \tag{2}$$

The desired control signal will be first converted to the reference current signals. By assuming the reference signal for i_d is $i_{q,\text{ref}} = 0$ (Eriksson, 2019), the reference signal of i_q can be therefore computed by using (2):

$$i_{q,\text{ref}} = -\sqrt{\frac{2}{3}} \frac{F_{\text{PTO,ref}}\, r_{\text{eq}}}{n_p} \cdot \frac{1}{\psi_f + (L_d - L_q) i_d} \tag{3}$$

where $i_{q,\text{ref}}$ is not directly used to solve for the reference signal i_q because the instantaneous i_d may not have converged to the reference signal. Once the reference control signal is converted to a reference current signal, a proportional-integral (PI) control law is employed to determine the required voltage input to the LEM:

$$\begin{aligned} v_d &= -K_{i,d} \int i_d \, dt - K_{p,d} \, i_d \\ v_q &= -K_{i,q} \int \left(i_q - i_{q,\text{ref}} \right) dt - K_{p,q} \left(i_q - i_{q,\text{ref}} \right) \end{aligned} \tag{4}$$

where $K_{i,d}$ and $K_{i,q}$ are the integral gains in the dq frame, respectively, and $K_{p,d}$ and $K_{p,q}$ are the proportional gains in the dq frame, accordingly. It is assumed that the required voltages v_d and v_q can be supported by the inverter:

$$i_{q,\text{ref}} = \begin{cases} \text{sign}\left(i_{q,\text{ref}} \right) i_{q,\max}, & \text{if } \left| i_{q,\text{ref}} \right| > i_{q,\max}, \\ (59), & \text{else.} \end{cases} \tag{5}$$

where $i_{\max}$ is the maximum current of the LEM. The generated electricity P_e can be computed as:

$$P_e = \sqrt{\frac{3}{2}} \left(v_d i_d + v_q i_q \right) \tag{6}$$

In the wave-to-wire model, the PTO force and the q-axis current are coupled through electromagnetic conversion (2), while the stator-voltage dynamics (1) bound the current slew via the inductive term $L_q \dot{i}_q$ and the back-EMF $\omega_e (L_d i_d + \psi_f)$. With $i_d \approx 0$ and the power-invariant $\sqrt{2/3}$ scaling, the torque-force map $u \approx -K_t i_q$ holds with $K_t = \frac{n_p}{r_{\text{eq}}} \sqrt{\frac{3}{2}} \psi_f$, and it follows that $\dot{u} \approx -K_t \dot{i}_q$ (the PTO force-rate, in discrete time

$\Delta u_k = u_k - u_{k-1}$). Enforcing the inverter box constraint ($|v_q| \le v_{q,\max}$) together with the hard current constraint ($|i_q| \le i_{q,\max}$) and the instantaneous speed $|\omega_e|$ gives $|\dot{i}_q| \le [\, v_{q,\max} - R_s|i_q| - |\omega_e|\psi_f \,]_+ / L_q$. Consequently, $|\dot{u}| \le (K_t/L_q)[\, v_{q,\max} - R_s|i_q| - |\omega_e|\psi_f \,]_+$. In discrete time this gives the implementable PTO force-rate constraint $|\Delta u_k| \le \dot{u}_{\max} T_s$. A PTO force trajectory is admissible only if the associated current and voltage remain within limits, so the amplitude bound $|u| \le u_{\max}$ alone is not sufficient. Accordingly, the voltage and current amplitude constraints are retained, and a hard rate limit on u is imposed to ensure electrical feasibility and actuator safety. The effective electrical damping grows with $|i_q|$ and $|\omega_e|$, which tightens the feasible rate.

2.2. State-space model

To achieve consistent modelling of the electrical and mechanical dynamics, this paper incorporates the electromagnetic thrust generated by the LEM into the mechanical dynamics model of the WEC. Based on the principle of electromagnetic energy conversion, the electromagnetic thrust generated by the LEM is determined by the q-axis current. Under common field-oriented control conditions, the thrust can be approximately linearised as ($F_{\text{PTO}} = k_t i_q$). k_t is the thrust constant, representing the electromagnetic thrust generated per unit current. Its magnitude depends on parameters such as the number of motor pole pairs, flux linkage, and equivalent radius. This thrust acts on the float in the opposite direction of the wave excitation force and represents the mechanical reaction force of the power take-off (PTO). Therefore, in the state-space model, the control input u is directly equivalent to the PTO force ($u = F_{\text{PTO}}$). The input term in (7) is the PTO reaction, which provides a direct mapping from (1)–(6) to (7). The state-space model can be represented by:

$$\dot{x} = A_c x + B_{uc} u + B_{wc} w \tag{7a}$$

$$v = C_v x \tag{7b}$$

$$z = C_z x \tag{7c}$$

where w is the wave excitation whose prediction is incorporated into the controller design, $x := [z_v, \dot{z}_v, x_r]$ represents the system state vector, $z := z_v$ is the vertical displacement, and $v := \dot{z}_v$ is the corresponding velocity. $(A_c, B_{uc}, B_{wc}, C_c)$ are:

$$A_c = \begin{bmatrix} 0 & 1 & 0 \\ -\frac{k_s}{m} & 0 & \frac{C_r}{m} \\ 0 & B_r & A_r \end{bmatrix} \quad B_{uc} = \begin{bmatrix} 0 \\ \frac{1}{m} \\ 0 \end{bmatrix} \quad B_{wc} = \begin{bmatrix} 0 \\ \frac{1}{m} \\ 0 \end{bmatrix} \quad C_c = \begin{bmatrix} 0 & 1 & 0_{1\times n_r} \end{bmatrix} \tag{8}$$

with $m := m_s + m_\infty$.

To formulate the MPC scheme, the continuous-time model (7) is discretised to obtain the discrete-time model (9):

$$x_{k+1} = A x_k + B_u u_k + B_w w_k \tag{9a}$$

$$z_k = C_z x_k \tag{9b}$$

$$v_k = C_v x_k \tag{9c}$$

where the quadruple (A, B_u, B_w, C) is the discrete-time form of the quadruple $(A_c, B_{uc}, B_{wc}, C_c)$. z_k represents the heave displacement, and v_k represents the heave velocity. Subsequent work will use this discrete-time model to develop linear optimal control for WECs.

2.3. Control optimisation problem

Based on the continuous-time WEC dynamics and constraints defined in Section 2.1, the corresponding discrete-time formulations are introduced for the control design. The output power and cumulative energy at time instant k are expressed as:

$$P_k := -v_k\, u_k \tag{10a}$$

$$E_k := -t_s \sum_{i=0}^{k} v_i u_i \tag{10b}$$

where the constraints of z_k, v_k, and u_k are expressed as:

$$|z_k| \le \Phi_{\max} \quad |v_k| \le v_{\max} \quad |u_k| \le u_{\max} \tag{11}$$

where $\Phi_{\max}$, $v_{\max}$, and $u_{\max}$ denote the maximum admissible float heave displacement, heave velocity, and maximal control input force acting on the piston, respectively. The voltage and current limits in the wave-to-wire model imply a finite admissible slew of the actuator-side force in discrete time. To encode this implementability requirement, the constraint set is augmented with a discrete rate limit on the control input:

$$\Delta u_k := u_k - u_{k-1}, \quad |\Delta u_k| \le \dot{u}_{\max}\, T_s \tag{12}$$

where T_s is the sampling period and $\dot{u}_{\max}$ is the admissible force slew rate determined from the electrical envelope (voltage/current limits). At the first sampling instant one can set $u_{-1} := u_0$ so that (12) is well-defined.

For a PTO with a ±3500 N limit and a system with a 0.1-second sampling rate, we know that ±7000 N per sample is a reasonable assumption. But this is a mathematical upper-bound if the PTO is allowed to use the full force range for every control step. In real wave-to-wire systems, the electrical limits (DC bus, back-EMF, inductance) usually make the true rate limit much lower than this. So based on the wave-to-wire model, we impose a tighter rate constraint (20-50 % of full swing per step), which is also the main contribution that distinguishes our work from Siyuan's previous publication. Therefore, in our simulation, we constrain the rate of PTO change to ±3500 N/step , which is 50 % of the full swing per step.

The objective of the WEC controller is to maximise the energy output defined in (10b), subject to the constraint in Section 3.1, that is, the maximum heave height profile satisfying:

$$|w| \le w_{\max} \tag{13}$$

with a n_p-step wave excitation force prediction:

$$\mathbf{w}_k = [w_{k|k}, w_{k+1|k}, \ \dots, \ w_{k+n_p+1|k}] \tag{14}$$

where $w_{\max}$ represents the maximum wave heave amplitude at which the WEC can safely operate. The non-causal optimal control problem for a WEC can be solved within the receding horizon framework of MPC by recursively solving the following constrained optimal control problem:

$$u_k^* = arg \min_{[u_{k|k}, \dots, u_{k+n_p-1|k}]} \sum_{i=0}^{n_p-1} v_{k+i|k} u_{k+i|k} \tag{15a}$$

$$s.t. (9),\ (12),\ (15c),\ (15d) \tag{15b}$$

$$|z_{k+i}| \le \Phi_{\max}, |v_{k+i}| \le v_{\max}, |u_{k+i}| \le u_{\max}, \tag{15c}$$

$$\forall |w_{k+i}| \le w_{\max}, \forall i \in I_{[0,n_p-1]} \tag{15d}$$

where the first element of u_k^* is applied as the control input at time instant k.

Unlike traditional MPC, which primarily relies on convex quadratic programming for state regulation and trajectory tracking, MPC applied to WEC aims to maximise energy output. Due to the high uncertainty of waves, its cost function $v_{k+i|k} u_{k+i|k}$ exhibits non-convex characteristics. WEC operates under periodic and highly uncertain sea conditions for a long time, making it difficult for the system state to converge to a fixed equilibrium point. The controller must not only ensure that the state and control inputs satisfy the constraints (11) under various incident wave conditions, but also continuously adhere to wave height limits (13) to ensure safe and reliable operation. WEC-MPC is a non-causal optimal control problem. By introducing short-term wave prediction w_k, the controller can actively adjust the control strategy. Compared to traditional MPC, which treats external disturbances as suppression targets, WEC uses incident waves as the primary energy source, and the control objective shifts from suppressing disturbances to actively enhancing energy absorption.

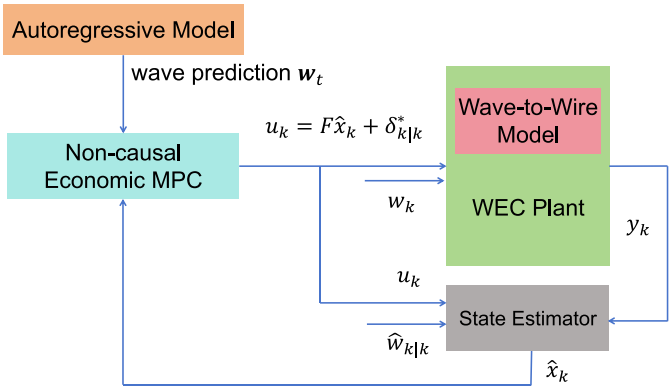

Fig. 3. WEC non-causal EMPC framework.

3. Non-causal EMPC structure design

This section describes the proposed non-causal EMPC. Section 3.1 explains the overall controller strategy. Section 3.2 introduces the EMPC architecture design. Section 3.3 presents a wave prediction method based on an autoregressive model.

3.1. Overall strategy

The proposed non-causal EMPC method is implemented within each sampling period. Based on the current measurable system state and wave forecast information, a prediction model is established and a finite-time optimisation problem is solved to obtain the optimal control input u_k. This input acts on the dynamic model of the float/actuator, updating the system state and serving as a coupling variable between the mechanical and electrical sides. By combining the motor and generator parameter relationships, the current i_k and voltage v_k are calculated, yielding instantaneous power and energy output for evaluating energy conversion performance. By simultaneously performing control optimisation and electrical performance evaluation in a unified control loop, this method quantitatively analyses the electromechanical energy conversion process based on the wave-to-wire model and updates control decisions in real time. Meanwhile, the state observer acts on the mechanical subsystem based solely on the measured displacement and velocity signals. Electrical variables such as current and voltage are regulated by fast internal control loops and are therefore not directly included in the state estimation process. Their impact on the mechanical dynamics is implicitly reflected through the power take-off (PTO) force, which serves as the control input in the state-space model. Under the receding-horizon implementation, the discrete rate constraint (12) is enforced at each sampling instant, ensuring that the applied control increments remain within the bound throughout the closed loop Fig. 3.

3.2. Economic model predictive control

Conventional MPC methods for WEC often encounter difficulties in guaranteeing recursive feasibility (Zhang et al., 2020). EMPC is introduced to overcome this limitation. In practical applications, not all states can be directly measured, and the non-causal and long-term memory characteristics of radiation dynamics exacerbate prediction errors. This paper employs an observer based on an autoregressive model to reconstruct the complete state from measurable signals to improve prediction accuracy. After obtaining the optimal control input, the EMPC framework is further combined with an independent wave-to-wire model to calculate the current, voltage, and power at the generator terminal, thereby enabling quantitative assessment of energy performance and feedback updates. Based on this, an integrated EMPC framework is proposed:

$$u_k = F\hat{x}_k + \delta_k \tag{16}$$

where F is the feedback gain designed offline, $\hat{x}$ is the estimated state, and δ is an auxiliary variable that requires online calculation. In the EMPC framework, the design of the feedback gain matrix F ensures system robustness under various sea conditions, thereby enhancing the wave energy system's adaptability. δ is obtained by solving an online optimisation problem that maximises energy output while satisfying system constraints.

Based on the available wave prediction (14), a Luenberger observer is designed to estimate the full information of the state, which is in the form of:

$$\hat{x}_{k+1} = A\hat{x}_k + B_u u_k + B_w w_{k|k} + L(y_k - C\hat{x}_k) \tag{17}$$

where $w_{k|k}$ is the estimation of current wave excitation and is defined in (14), y_k is the measured output:

$$y_k = Cx_k \tag{18}$$

where $C := [C_z, C_v]$, C_z and C_v are defined as in (7). Assume A, C are observable. The observer gain L must satisfy $\rho(A - LC) < 1$ to ensure that the estimated state $\hat{x}_k$ can effectively reconstruct the actual state x_k within the allowable error range ($\xi_k := x_k - \hat{x}_k$). Due to the presence of input and state constraints, the traditional controller-observer separation principle is no longer directly applicable. Therefore, the impact of state estimation on the closed-loop system must be explicitly considered in controller design to avoid constraint violations. Comparing (9) with (18) yields:

$$\xi_{k+1} = (A - LC)\xi_k + B_u u_k + B_w(w_k - w_{k|k}) \tag{19}$$

Since $\rho(A - LC) < 1$, there exists a bounded set $\mathbb{E}$ such that for all $k \geq 0$, $\xi_k \in \mathbb{E}$ (Mayne et al., 2006). When $k \to \infty$, the estimated error $\xi_k \to 0$, and $w_{k|k} = w_k$. Since the systems A, C are observable and the observer poles can be placed at the desired locations by adjusting L, this paper assumes that the observer gain design ensures that $\mathbb{E}$ is sufficiently small. According to observer design principles, while larger gains can accelerate error convergence, they also increase the demand for computational resources. Therefore, in practical applications, a trade-off must be struck between convergence velocity and real-time performance. Although a numerically tractable MPC algorithm can be constructed based on Eq. (15) and combined with incident wave preview information (Li and Belmont, 2014), its recursive feasibility cannot be guaranteed.

In order to explicitly characterise the bounded estimation error, the set $\mathbb{E}$ is defined as the minimal robust positively invariant (mRPI) set of the error dynamics (19), namely $\mathbb{E} = \{\xi \in \mathbb{R}^{n_x} \mid (A - LC)\xi + B_w\tilde{w} \in \mathbb{E},\ \forall \tilde{w} \in \mathbb{W}\}$. It can be iteratively computed by $\mathbb{E}_{i+1} = (A - LC)\mathbb{E}_i \oplus B_w\mathbb{W}$ with $\mathbb{E}_0 = \{0\}$ until $\mathbb{E}_{i+1} \subseteq \mathbb{E}_i$, yielding a compact polyhedral set that bounds all feasible estimation errors under the bounded disturbance $\mathbb{W}$. $\mathbb{E}$ obtained by this fixed-point iteration is numerically incorporated into the constraint tightening in (22). Physically, $\mathbb{E}$ describes the admissible region of estimation uncertainty.

Following the recent analysis of García-Violini et al. (2024), the performance of structure-based excitation-force estimators critically depends on the spectral characteristics of the assumed disturbance model A_e. While harmonic-oscillator estimators can achieve perfect convergence for purely periodic waves, they tend to amplify high-frequency components and become numerically ill-conditioned when their assumed excitation frequency is large. Conversely, the random-walk formulation ($A_e = 0$) offers superior robustness in broadband, stochastic seas by avoiding such spectral amplification. In light of these findings, the proposed Luenberger observer adopts a low-gain configuration so that the eigenvalues of $(A - LC)$ remain within a moderate region of the unit circle, thereby limiting the closed-loop bandwidth and maintaining numerical stability. This treatment ensures that the tightened constraints in (22) remain robust under model mismatch and parameter drift, keeping the closed-loop system recursively feasible.

Table 1
Notation of sets (property and symbol).

Property (with units)	Symbol
State admissible set (components include displacement [m] and velocity [m/s])	$\mathbb{X}$
Input admissible set (control force [N])	$\mathbb{U}$
Bounded disturbance set (wave excitation force [N])	$\mathbb{W}$
Estimation-error set (same physical units as the state vector)	$\mathbb{E}$
Accumulated disturbance / tube set at prediction step i (state space)	$\mathbb{D}_i$
Terminal set; maximal output admissible set under bounded disturbances (state space)	Σ

For clarity, Table 1 summarises the set notation and units. To facilitate constraint handling, the state and input constraints and perturbation bounds are expressed as $x \in \mathbb{X}$, $u \in \mathbb{U}$, $w \in \mathbb{W}$, respectively, where $\mathbb{X}$, $\mathbb{U}$, and $\mathbb{W}$ are defined as follows:

$$\begin{aligned}\mathbb{X} &:= \left\{x \in \mathbb{R}^{n_x} \mid |C_z x_k| \le \Phi_{\max},\ |C_v x_k| \le v_{\max}\right\}\\ \mathbb{U} &:= \left\{u \in \mathbb{R} \mid |u_k| \le u_{\max}\right\}\\ \mathbb{W} &:= \left\{w \in \mathbb{R} \mid |w_k| \le w_{\max}\right\}\end{aligned} \tag{20}$$

where C_z and C_w are defined in (7), $\Phi_{\max}$ and $v_{\max}$ are defined in (11), and $w_{\max}$ is defined in (13). To ensure that the constraints given in (11) are satisfied and to guarantee recursive feasibility, the constraint in (15c) is further imposed for all $i \ge 0$.

The satisfaction of $x_{k+i} \in \mathbb{X}$ and $u_{k+i} \in \mathbb{U}$ for all $i \ge 0$ and for any incoming wave profile $w_{k+i} \in \mathbb{W}$ under given sea conditions can be ensured by introducing tightened constraints. The predicted auxiliary state and input trajectories are required to satisfy $\bar{x}_{k+i|k} \in \mathbb{X}_i$ and $\bar{u}_{k+i|k} \in \mathbb{U}_i$ for $i \in \mathcal{I}[0, n_p - 1]$, and $\bar{x}_{n_p+k|k} \in \mathbb{X}_T$, where these trajectories are obtained from the auxiliary system defined below:

$$\begin{aligned}\bar{x}_{k+i+1|k} &= A\bar{x}_{k+i|k} + B_u\bar{u}_{k+i|k}\\ \bar{u}_{k+i|k} &= F\bar{x}_{k+i|k} + \delta_{k+i|k}\\ \bar{x}_{k|k} &= \hat{x}_k\end{aligned} \tag{21}$$

where $\hat{x}_k$ denotes the state estimate generated by the Luenberger observer in (17), and the tightened constraint sets are specified as follows:

$$\mathbb{X}_i := \mathbb{X} \sim \mathbb{E} \sim \mathbb{D}_i, \quad \mathbb{U}_i := \mathbb{U} \sim F\mathbb{D}_i,$$

$$\mathbb{D}_i := \sum_{j=0}^{i-1} A_F^j\left[B_w\mathbb{W} \oplus (A_L - A_F)\mathbb{E}\right], \quad \mathbb{X}_T := \Sigma \sim \mathbb{D}_{n_p} \tag{22}$$

where $A_F := A + B_uF$, $A_L := A - LC$; $\mathbb{X}$, $\mathbb{U}$, and $\mathbb{W}$ are defined in (20); Σ is the maximal output admissible set (MOAS) defined by:

$$\Sigma := \left\{ \begin{array}{c} x_{k+1} = A_F x_k + \eta_k \\ x_0 \in \mathbb{X} :\ x_k \in \mathbb{X} \sim \mathbb{E},\ \ u_k \in \mathbb{U},\ \ \forall k \in \mathbb{I}_{\ge 0} \\ \forall\, \eta_k \in B_w\mathbb{W} \oplus (A_L - A_F)\mathbb{E} \end{array} \right\} \tag{23}$$

Following the robust MPC formulation proposed by Mayne et al. (2006), the recursive feasibility and closed-loop stability of the proposed EMPC are analysed as follows.

To formally guarantee recursive feasibility, consider the closed-loop error dynamics:

$$e_{k+1} = (A + B_uF)e_k + B_w w_k \tag{24}$$

where $e_k := x_k - \bar{x}_{k|k}$ denotes the deviation between the actual and nominal states. If there exists a compact set $\mathbb{S}$ satisfying the robust positive invariance condition:

$$(A + B_uF)\mathbb{S} \oplus B_w\mathbb{W} \subseteq \mathbb{S} \tag{25}$$

then $\mathbb{S}$ is a mRPI set for the closed-loop error dynamics. By tightening the feasible regions as:

$$\mathbb{Z} := \mathbb{X} \ominus \mathbb{S} \qquad \mathbb{V} := \mathbb{U} \ominus F\mathbb{S} \tag{26}$$

where $\mathbb{Z}$ and $\mathbb{V}$ denote the tightened set of state and input constraints, eliminating biases due to bounded disturbances and estimation errors. The feasibility of the nominal optimisation problem at time k implies its feasibility at time $k+1$. If $\bar{x}_k \in \mathbb{Z}$ and $\bar{u}_k \in \mathbb{V}$ at time k, then $\bar{x}_{k+1} \in \mathbb{Z}$ and $\bar{u}_{k+1} \in \mathbb{V}$, ensuring recursive feasibility of the EMPC under bounded disturbances.

Furthermore, to demonstrate closed-loop stability, define the quadratic Lyapunov function:

$$V(e_k) = e_k^{\mathsf{T}} P e_k, \qquad P > 0 \tag{27}$$

If there exists P satisfying the discrete Lyapunov inequality:

$$(A + B_uF)^{\mathsf{T}} P(A + B_uF) - P \le -Q, \qquad Q > 0 \tag{28}$$

then $V(e_{k+1}) - V(e_k) \le -e_k^{\mathsf{T}} Q e_k < 0$ for all $e_k \ne 0$, indicating that the error e_k asymptotically converges to the origin. Consequently, the closed-loop state $x_k = \bar{x}_{k|k} + e_k$ remains bounded within the invariant tube $\mathbb{S}$, while satisfying $x_k \in \mathbb{X}$ and $u_k \in \mathbb{U}$ for all k. Hence, both recursive feasibility and asymptotic Lyapunov stability of the EMPC framework are theoretically ensured.

Algorithm 1 Iterative computation of the estimation-error set $\mathbb{E}$ (mRPI).

Require: A; C; L; B_w; $\mathbb{W}$.
Ensure: The mRPI $\mathbb{E}$ for error dynamics $e_{k+1} = (A - LC)e_k + B_w w_k,\ w_k \in \mathbb{W}$.
1: Initialisation: Set $\mathbb{E}_0 \leftarrow \{0\}$.
2: **for** $i = 0, 1, 2, \ldots$ **do**
3: Update: $\mathbb{E}_{i+1} \leftarrow (A - LC)\mathbb{E}_i \oplus B_w\mathbb{W}$.
4: Convergence check: if $\mathbb{E}_{i+1} \subseteq \mathbb{E}_i$ then break.
5: **end for**
6: Return: $\mathbb{E} \leftarrow \mathbb{E}_{i+1}$.

By comparing (21) with (9), it follows that:

$$\begin{aligned}x_{k+i} &= \bar{x}_{k+i|k} + \xi_{k+i|k} + \sum_{j=1}^{i} A_F^{j-1} B_w\, w_{k+j}\\ u_{k+i} &= \bar{u}_{k+i|k} + F\left(\sum_{j=1}^{i} A_F^{j-1} B_w\, w_{k+j}\right)\end{aligned} \tag{29}$$

The tightened constraints in (22) are met by the state and input trajectories determined by (21), $x_{k+i} - \xi_{k+i|k} \in X \sim E$ and $u_{k+i} \in U$ for all $i \in \mathcal{I}[0, n_p - 1]$, and $x_{k+n_p} - \xi_{k+n_p|k} \in \Sigma$. By selecting the terminal local controller $u_{k+i} = Fx_{k+i}$ for $i \ge n_p$ and invoking the definition in (23), it follows that for all $i \in \mathcal{I}_{\ge 0}$, $x_{k+i} \in X$ and $u_{k+i} \in U$:

$$x_{k+i} - \xi_{k+i|k} \in \mathbb{X} \sim \mathbb{E}, \qquad u_{k+i} \in \mathbb{U} \tag{30}$$

Since the state estimation error satisfies $\xi_{k+i|k} \in E$, for all $i \in \mathcal{I} \ge 0$, $xk + i \in X$ and $u_{k+i} \in U$. If the feedback gain F is designed such that $\rho(A + B_uF) < 1$, the MOAS in (23) is a polyhedron and can be computed in a finite number of steps according to Kolmanovsky and Gilbert (1995). The detailed computational procedure is summarised in Algorithms 1 and 2.

Numerically, the computation was implemented using the MPT3 toolbox. A less conservative (larger) Σ enlarges the feasible region but reduces robustness to model mismatch. A smaller Σ ensures stronger constraint satisfaction but sacrifices the size of the feasible region. To maximise the safe operating range of the sea state sensor, F should be

Algorithm 2 Iterative computation of the maximal output admissible set Σ (MOAS).

Require: $\mathbb{X}$; $\mathbb{E}$; A_F; A_L; B_w; $\mathbb{W}$.
Ensure: Maximal output admissible set Σ for the disturbed/estimated closed-loop dynamics.
1: Initialisation: $\Sigma_0 \leftarrow \mathbb{X} \sim \mathbb{E}$.
2: **for** $i = 0, 1, 2, \ldots$ **do**
3: Disturbance/estimation aggregation: $\mathbb{D} \leftarrow B_w\mathbb{W} \oplus (A_L - A_F)\mathbb{E}$.
4: Update:

$$\Sigma_{i+1} \leftarrow \left\{ x \in \mathbb{X} \sim \mathbb{E} \;\middle|\; A_F x + \eta \in \Sigma_i,\ \forall \eta \in \mathbb{D} \right\}.$$

5: Convergence check: **if** $\Sigma_{i+1} \subseteq \Sigma_i$ then break.
6: **end for**
7: Return $\Sigma \leftarrow \Sigma_{i+1}$.

selected to ensure that the resulting MOAS lies below the maximum disturbance bound $w_{\max}$:

$$\max_F \ w_{\max}, \quad \text{s.t. } \exists\, \Sigma \text{ satisfies(23)} \tag{31}$$

The constrained optimisation problem generated by the original objective function defined in (15b) is generally non-convex, which leads to excessive computational complexity. Directly adopting the original objective function may result in optimal control being achieved using only the upper and lower limits of the control input. Frequent switching between extreme values increases the complexity of control implementation. Research (Li and Belmont, 2014) has demonstrated that solving the non-convex problem by appropriately modifying the objective function can significantly influence the control performance. In order to solve the problem caused by non-convexity, the objective function is convexified in an optimal way:

$$\sum_{i=0}^{n_p-1} \left(\tilde{u}_{k+i|k}\, C_v \tilde{x}_{k+i|k} \ + \ r\, \tilde{u}^2_{k+i|k} \right) \tag{32}$$

where the predicted trajectories $\tilde{x}_{k+i|k}$ and $\tilde{u}_{k+i|k}$ are computed from an auxiliary system:

$$\begin{aligned} \tilde{x}_{k+i+1\,|\,k} &= A\, \tilde{x}_{k+i\,|\,k} + B_u\, u_{k+i\,|\,k} + B_w\, w_{k+i\,|\,k} \\ \tilde{u}_{k+i\,|\,k} &= F\, \tilde{x}_{k+i\,|\,k} + c_{k+i\,|\,k} \\ \tilde{x}_{k\,|\,k} &= \hat{x}_k \end{aligned} \tag{33}$$

which can be rewritten in a compact form as:

$$\delta_k^{\top} \mathbf{H}\, \delta_k \ + \ \delta_k^{\top} \mathbf{F} \ + \ \mathbf{G} \tag{34}$$

where $\delta_k := [\, \delta_{k|k}, \ldots, \delta_{k+n_p-1|k} \,]^{\top}$. Coefficients $\mathbf{H}$, $\mathbf{F}$, and $\mathbf{G}$ are determined by straightforward matrix manipulations. From (33), the predicted heave-velocity and control-input trajectories are $v_k := [C_v x_{k|k}, \ldots, C_v \tilde{x}_{k+n_p-1|k}]$ and $u_k := [u_{k|k}, \tilde{u}_{k+1|k}, \ldots, \tilde{u}_{k+n_p-1|k}]$, which are calculated by the following formulas:

$$\tilde{\mathbf{v}}_k = M_v \hat{x}_k + C_{cv} \boldsymbol{\delta}_k + C_{wv} \mathbf{w}_k, \quad \tilde{\mathbf{u}}_k = M_u \hat{x}_k + C_{cu} \boldsymbol{\delta}_k + C_{wu} \mathbf{w}_k \tag{35}$$

where

$$M_v := \begin{bmatrix} C_v \\ C_v A_F \\ \vdots \\ C_v A_F^{n_p-1} \end{bmatrix} \quad M_u := \begin{bmatrix} I \\ F A_F \\ \vdots \\ F A_F^{n_p-1} \end{bmatrix}$$

$$C_{cv} := \begin{bmatrix} 0 & & & & \\ C_v B_u & 0 & & & \\ C_v A_F B_u & C_v B_u & 0 & & \\ \vdots & \vdots & \vdots & \ddots & \\ C_v A_F^{n_p-2} B_u & \cdots & C_v A_F B_u & C_v B_u & 0 \end{bmatrix}$$

$$C_{wv} := \begin{bmatrix} 0 & & & & \\ C_v B_w & 0 & & & \\ C_v A_F B_w & C_v B_w & 0 & & \\ \vdots & \vdots & \vdots & \ddots & \\ C_v A_F^{n_p-2} B_w & \cdots & C_v A_F B_w & C_v B_w & 0 \end{bmatrix}$$

$$C_{cu} := \begin{bmatrix} 1 & 0 & & & \\ F B_u & 1 & 0 & & \\ F A_F B_u & F B_u & 1 & 0 & \\ \vdots & \vdots & \vdots & \ddots & \\ F A_F^{n_p-2} B_u & \cdots & F A_F B_u & F B_u & 1 \end{bmatrix}$$

$$C_{wu} := \begin{bmatrix} 0 & & & & \\ F B_w & 0 & & & \\ F A_F B_w & F B_w & 0 & & \\ \vdots & \vdots & \vdots & \ddots & \\ F A_F^{n_p-2} B_w & \cdots & F A_F B_w & F B_w & 0 \end{bmatrix}$$

where $A_F := A + B_u F$ and (32) can be written in matrix multiplications $r\tilde{\mathbf{u}}_k^T \tilde{\mathbf{u}}_k + \tilde{\mathbf{u}}_k^T \tilde{\mathbf{v}}_k$. With (35), the $\mathbf{H}$, $\mathbf{F}$, and $\mathbf{G}$ in (34) can be determined by:

$$\mathbf{H} = r\, C_{cu}{}^{\top} C_{cu} + \frac{1}{2} \left(C_{cu}{}^{\top} C_{cv} + C_{cv}{}^{\top} C_{cu} \right) \tag{36}$$

$$\mathbf{F} = \left(C_{cv} + r\, C_{cu} \right)^{\top} \left(M_u \hat{\mathbf{x}}_k + C_{wu} \mathbf{w}_k \right) + C_{cu}{}^{\top} \left(M_v \hat{\mathbf{x}}_k + C_{wv} \mathbf{w}_k \right) \tag{37}$$

$$\begin{aligned} \mathbf{G} = &\left(M_u \hat{\mathbf{x}}_k + C_{wu} \mathbf{w}_k \right)^{\top} \left(M_v \hat{\mathbf{x}}_k + C_{wv} \mathbf{w}_k \right) \\ &+ r \left(M_v \hat{\mathbf{x}}_k + C_{wv} \mathbf{w}_k \right)^{\top} \left(M_v \hat{\mathbf{x}}_k + C_{wv} \mathbf{w}_k \right) \end{aligned} \tag{38}$$

Compared with the original stage cost (15a), the modified stage cost (32) introduces a regularisation term to enforce convexity of the quadratic program. To achieve a balance between convexity assurance and control performance, the coefficient r should be selected such that convexity is guaranteed while energy capture is maximised. In this study, the optimisation framework leads to an optimal value of $r^{\star} = 1.788 \times 10^{-4}$, which achieves the best trade-off between numerical convexity and energy output in simulations:

$$\min_{r \geq 0} |r|, \quad \text{s.t. } \mathbf{H} \succeq 0 \tag{39}$$

3.3. Wave prediction by autoregressive model

Recursive least squares (RLS) is a widely adopted parameter estimation algorithm, and it is applied to train an autoregressive model for wave data prediction with the aim of minimising the model error. The sampling time is T_s, with training and prediction durations of T_{train} and T_{predict}, respectively. A 1-second prediction phase is carried out after every 5-second training cycle. The total prediction time is expressed as T_{total}. Each prediction horizon contains N_{pred} prediction points. The training-prediction cycle time offset N_{shift} is the time interval between the training and the prediction. The initial regularisation coefficient is α_{base}. To ensure that the training data remains uniform in scale, the data is processed by normalisation:

$$\tilde{w} = \frac{w - \mu}{\sigma} \tag{40}$$

where $\tilde{w}$ denotes the standardised training value, μ and σ are the mean and standard deviation of w, respectively. Before performing multi-step prediction, an initial input vector ϕ is initialised, which contains past observations required for prediction. The input vector is defined as:

$$\phi = \begin{bmatrix} \tilde{w}_{N_{\text{train}}} & \tilde{w}_{N_{\text{train}}-1} & \cdots & \tilde{w}_{N_{\text{train}}-p+1} \end{bmatrix}^{\top} \tag{41}$$

where the first p data points from the training data are flipped to construct the input vector ϕ of the autoregressive model, p is the order of the autoregressive model, implying that each subsequent prediction relies on previous p data points. The predicted value is expressed as:

$$w_{\text{pred}} = \theta \phi \tag{42}$$

where w_{pred} denotes the predicted value, and the parameter vector θ represents the model weights, initially assigned as a zero vector. θ is updated progressively to minimise the prediction error by using the RLS algorithm. The predicted error e_{pred} is formulated as:

$$e_{\text{pred}} = \tilde{w} - w_{\text{pred}} \tag{43}$$

where e_{pred} denotes the predicted error, defined as the difference between the predicted and the actual values. Through this procedure, the multi-step prediction results can be obtained for a specified time horizon:

$$\alpha_{\text{dynamic}} = \alpha_{\text{dynamic}}(1 + |e_{\text{pred}}|) \tag{44}$$

where the dynamic regularisation coefficient α_{dynamic} is initialised as α_{base}. α_{dynamic} is adapted to regulate the update strength at each step. When $|e_{\text{pred}}|$ is large, α_{dynamic} is increased to the magnitude of parameter updates. The Kalman gain K is expressed as:

$$K = \frac{P\phi'}{\lambda_{\text{rls}} + \phi P \phi' + \alpha_{\text{dynamic}} + l} \tag{45}$$

where $P\phi'$ denotes the incremental information derived from the past, the denominator incorporates both the forgetting factor λ_{rls} and the regularisation term, ensuring stability of the update. λ_{rls} mitigates the influence of old data. P represents the covariance matrix employed for updating the parameter calculations. The regularisation parameter l is introduced to prevent overfitting. The parameter update equation for θ is expressed as:

$$\theta_k = \theta_{k-1} + K e_{k,\text{pred}} \tag{46}$$

The covariance matrix P is updated according to:

$$P_k = \frac{(1 - K\phi_{k-1})P_{k-1}}{\lambda_{\text{rls}}} \tag{47}$$

where P progressively converges over time, diminishing the model's sensitivity to historical data while improving both the stability and accuracy of predictions:

$$E_{\text{cv}}^{(p)} = \frac{1}{N_{\text{train}} - p} \sum_{k=p+1}^{N_{\text{train}}} |e_{\text{pred}}| \tag{48}$$

where $E_{\text{cv}}^{(p)}$ represents the cross-validation error of the autoregressive model of order p, serving as a metric for model fitting performance across different orders: smaller values indicate superior model fitting, N_{train} is the total number of training samples, $N_{\text{train}} - p$ is the number of observations employed in error computation, and k is the index variable ranging from $p+1$ to N_{train}, ensuring that sufficient past data are available for prediction.

Traditional modelling sequential estimation methods include the Akaike Information Criterion (AIC) and the Bayesian Information Criterion (BIC) (Atyabi et al., 2016). AIC avoids overfitting and penalises complex models through a trade-off between accuracy of fit and model complexity:

$$AIC_p = N_{\text{train}} \log\left(\frac{1}{N_{\text{train}}} \sum_{k=p+1}^{N_{\text{train}}} e_{\text{pred}}^2\right) + 2p \tag{49}$$

$$BIC_p = N_{\text{train}} \log\left(\frac{1}{N_{\text{train}}} \sum_{k=p+1}^{N_{\text{train}}} e_{\text{pred}}^2\right) + p\log(N_{\text{train}}) \tag{50}$$

where AIC_p and BIC_p represent the AIC and BIC values, respectively, for an autoregressive model with order p, a smaller value indicates a better fit, N_{train} denotes the number of training samples, log is employed to capture data growth rates and evaluate model complexity, $\sum_{k=p+1}^{N_{\text{train}}} e_{\text{pred}}^2$ is the sum of squares of prediction errors, $2p$ denotes the penalty term for model complexity in AIC, and $p\log(N_{\text{train}})$ denotes the penalty term in BIC, which increases with the sample size. BIC imposes stronger penalties on higher-order models and thus tends to select simpler models to avoid overfitting. Compared with AIC, BIC is stricter in penalizing complex models.

To implement multi-step prediction, the initial predicted value $\hat{w}_{1,\text{pred}}$ is appended to the input vector ϕ_{pred} and treated as the most recent observation for subsequent multi-step predictions:

$$\phi_{\text{pred}} = \begin{bmatrix} \hat{w}_{1,\text{pred}} & \tilde{w}_{N_{\text{train}}} & \tilde{w}_{N_{\text{train}}-1} & \cdots & \tilde{w}_{N_{\text{train}}-p+2} \end{bmatrix}^{\top} \tag{51}$$

Multi-step prediction is carried out using the parameter vector θ and the input vector ϕ_{pred}. The corresponding model output $\hat{w}_{\text{pred}}$ is obtained as:

$$\hat{w}_{\text{pred}} = \theta\phi_{\text{pred}} \tag{52}$$

where $\hat{w}_{\text{pred}}$ denotes the predicted normalised value. For multi-step prediction, the prediction output is recursively fed back, and the input vector is updated at each step k:

1. Generate the new prediction (52).
2. Update ϕ_{pred}:

$$\phi_{\text{pred}} = \begin{bmatrix} \hat{w}_{1,\text{pred}} & \phi_{1:\text{end}-1,\text{pred}} \end{bmatrix}^{\top} \tag{53}$$

where the input vector ϕ_{pred} incorporates the most recent predicted value together with the past actual observations. After multi-step predictions, the predicted results are denormalised to convert the normalised predictions back to the original scale:

$$\bar{w} = \hat{w}_{\text{pred}}\sigma + \mu \tag{54}$$

where $\bar{w}$ denotes the prediction result after denormalisation. For the first prediction, the predicted segment is appended directly to the overall results. For subsequent predictions, continuity is maintained by setting the initial value of the new segment equal to the last predicted value of the preceding segment, after which the segments are concatenated:

$$w_{\text{p,all}} = [w_{\text{p,all}}, \bar{w}] \tag{55}$$

where $w_{\text{p,all}}$ denotes the cumulative predicted value. Following each prediction, the timestamp is updated accordingly:

$$t_{\text{p,all}} = [t_{\text{p,all}}, t_{\text{pi}}] \tag{56}$$

where $t_{\text{p,all}}$ denotes the cumulative predicted time, and t_{pi} represents the time series of the current predicted segment.

Table 2
QP characteristics and computation performance of the proposed EMPC.

Property	Value
Solver type	Active-set QP (`quadprog`)
Decision variables	10
Linear constraints	2
Hessian condition number	2.85×10^3
Positive definiteness	Yes
Average computation time	3.3 ms
Maximum computation time	151.6 ms
Warm-start usage	No
Sampling period	0.1 s
Hardware platform	Lenovo ThinkPad X13 Gen 2 (Intel i7, 1.9 GHz)

4. Simulation results and analysis

Table 2 This section shows the simulation results generated using MATLAB R2023b. The computer model is the Lenovo ThinkPad X13 Gen 2. This paper uses real wave data collected from the coast of Cornwall, UK. The state space matrix of the impulse function for calculating the radiation force is:

$$A_r = \begin{bmatrix} 0 & 0 & -17.9 \\ 1 & 0 & -17.7 \\ 0 & 1 & -4.41 \end{bmatrix} \quad B_r = \begin{bmatrix} 36.5 \\ 394 \\ 75.1 \end{bmatrix} \quad C_r = \begin{bmatrix} 0 & 0 & 1 \end{bmatrix}$$

The system is discretised with a sampling time of $t_s = 0.1$ s, and the non-causal EMPC is constructed using the Algorithm 3. At each sampling

Algorithm 3 Implementation of the non-causal EMPC (active-set QP solver, MATLAB `quadprog`).

1: Obtain the short-time incoming wave prediction w_k from the autoregressive model.
2: Update the state estimation:

$$\hat{x}_k = \hat{x}_{k|k-1} + L\big(y_k - C\hat{x}_{k|k-1}\big) \tag{57}$$

where $\hat{x}_{k|k-1}$ is the estimated state computed at the previous time instant $k-1$.
3: Compute the optimal control correction by solving the following quadratic program:

$$\boldsymbol{\delta}_k^* = \arg\min_{\boldsymbol{\delta}_k} \ \boldsymbol{\delta}_k^{\mathsf{T}}\mathbf{H}\boldsymbol{\delta}_k + \boldsymbol{\delta}_k^{\mathsf{T}}\mathbf{F} \quad \text{s.t. (21) and (22)} \tag{58}$$

4: Solve (58) and apply the control input $u_k = F\hat{x}_k + \delta^*_{k|k}$, where $\delta^*_{k|k}$ is the first element of δ_k^*.
5: Compute the reference signal of i_q and v_q:

$$i_{q,\mathrm{ref}} = -\sqrt{\frac{2}{3}}\,\frac{F_{\mathrm{PTO,ref}}\, r_{\mathrm{eq}}}{n_p\big(\psi_f + (L_d - L_q)i_d\big)} \tag{59}$$

$$v_q = -K_{i,q}\int \big(i_q - i_{q,\mathrm{ref}}\big)\mathrm{d}t - K_{p,q}\big(i_q - i_{q,\mathrm{ref}}\big) \tag{60}$$

6: Update the state prediction:

$$\hat{x}_{k+1|k} = A\hat{x}_k + B_u\, u_k + B_w\, w_{k|k} \tag{61}$$

where $w_{k|k}$ denotes the current wave measurement/prediction consistent with the AR model.
7: Proceed to the next time instant $k+1$ and repeat steps 1 to 5.

Note (solver setup & timing). Each control step constructs the QP and solves it with MATLAB `quadprog` (active-set, no warm start). In MATLAB R2023b on a ThinkPad X13 Gen 2 (Intel i7, 1.9 GHz), the mean and worst-case solve times are 3.3 ms and 151.6 ms, respectively. Occasional peaks stem from constraint switching, while the average remains well below the 0.1 s sampling period, confirming real-time feasibility. Considering desktop-embedded performance differences, the estimated execution on an ARM target also fits within the 0.1 s budget. Further solver characteristics are summarised in Table 2.

time, using wave prediction techniques, the incident wave excitation of $t_p = 1$ s (corresponding to $n = 10$ prediction steps) can be obtained. The observer gain L is designed as:

$$L = \begin{bmatrix} 0.9412 & -1.1639 & 0.5283 & -20.5234 & -4.4657 \\ 0.0980 & 0.9400 & -3.1529 & 31.9104 & 7.4290 \end{bmatrix}^{\mathrm{T}}$$

Assuming that the estimation error of the ocean current wave excitation force satisfies $|w_{k|k} - w_k| \le 0.1\, w_{\max}$, the error bound $E = \{e \in \mathbb{R}^5 : |C_z e| \le 0.01\}$ is obtained. The feedback gain F is designed as:

$$[F = -416.61 \quad -1025.57 \quad 0.1225 \quad -0.4785 \quad 0.9963] \tag{62}$$

and the maximum wave excitation boundary for MOAS Σ is $w_{\max} = 3.52$ kN. The non-causal EMPC can operate safely in all sea conditions where the maximum wave excitation does not exceed 3.52 kN.

To facilitate the design of non-causal EMPC, (22) is used to compute the tightened state constraints $\mathbb{X}_k$, input constraints $\mathbb{U}_k$, and the terminal constraint set $\mathbb{X}_T$ for $k \in \mathbb{I}_{[0,9]}$. Fig. 4 shows the projection of $\mathbb{X}_k$ onto the x_1-x_2 plane. The contour lines correspond to the continuously tightened feasible region, with the outermost boundary corresponding to $\mathbb{X}_0$ and the innermost boundary corresponding to $\mathbb{X}_9$. As k increases, the set gradually shrinks, reflecting the gradual narrowing of the feasible state domain. Its symmetry about the two coordinate axes reflects the constraint balance in the x_1 and x_2 directions. The figure also shows the projection of the tightened terminal set $\mathbb{X}_T$ onto the x_1-x_2 plane. Since the system is of fifth order, direct visualisation in the full state space is not feasible, so a two-dimensional projection is used to highlight key features. The closed contour lines define a compact, symmetric, and smoothly bounded feasible terminal region, thus ensuring terminal constraints, closed-loop stability, and constraint satisfaction Tables 3,4 and 12.

To ensure a fair comparison, the conventional MPC and the proposed non-causal EMPC use the same model dynamics, state and input

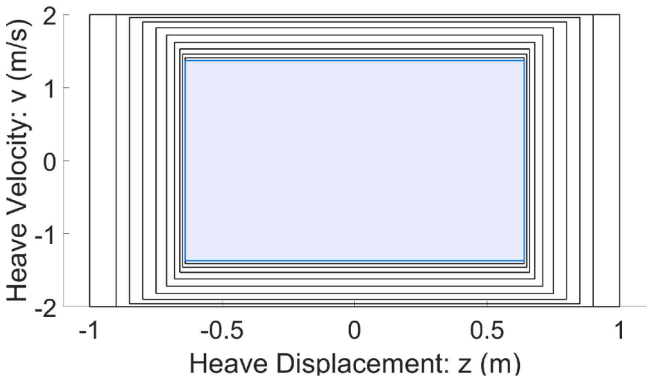

Fig. 4. Projection of the tightened state constraints on the x_1-x_2 plane. The contour lines from outside to inside represent $X_0, X_1, \ldots, X_9$.

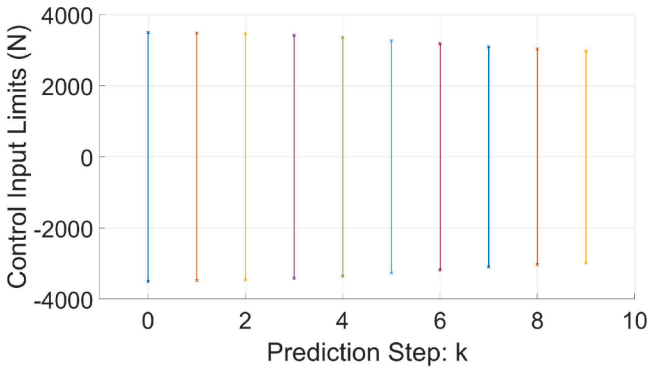

Fig. 5. Tightened control input constraint sets U_k for $k \in \mathbb{I}_{[0,1,\ldots,9]}$.

Table 3
Physical parameters of autoregressive model.

Description	Notation	Value
Forgetting factor	λ_{rls}	0.99
Initial regularisation coefficient	α_{base}	10^{-8}
Regularisation parameter	ℓ	10^{-8}
Sampling time	T_s	0.1 s
Training duration	T_{train}	5 s
Prediction duration	T_{predict}	1 s
Total prediction time	T_{total}	200 s
Prediction points	N_{pred}	11
Cycle time offset	N_{shift}	10
Covariance matrix	P	$10^7 \times I_p$
Identity matrix	I_p	$\mathrm{diag}(1,\ldots,1)_{p\times p}$

Table 4
Physical parameters of the WEC model.

Description	Notation	Value
Float mass	m_s	242 kg
Added mass	m	83.5 kg
Total mass	m	325.5 kg
Stiffness	k_s	3866 N/m
Control input limit	$u_{\max}$	3.5 kN
Heave displacement limit	$\Phi_{\max}$	1 m
Heave velocity limit	$v_{\max}$	2 m/s
Control input rate limit	$\dot{u}_{\max}$	3.5 kN/s

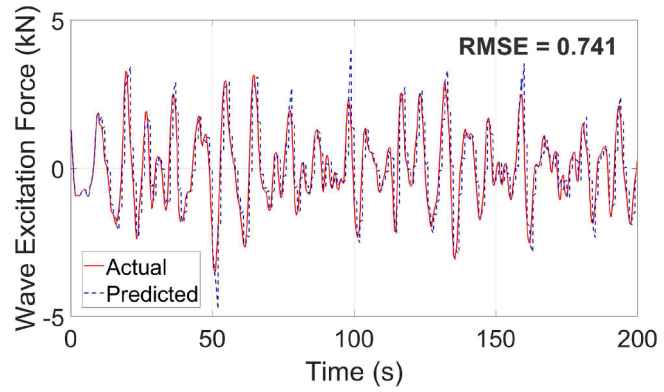

Fig. 6. Comparison of actual and predicted wave excitation forces. The solid red line represents the actual data, and the dashed blue line represents the predicted data. Forces are expressed in Newtons (kN), and time is expressed in seconds (s). The root mean square error (RMSE) of the predicted values is 0.741 demonstrating excellent agreement between the actual and predicted data.

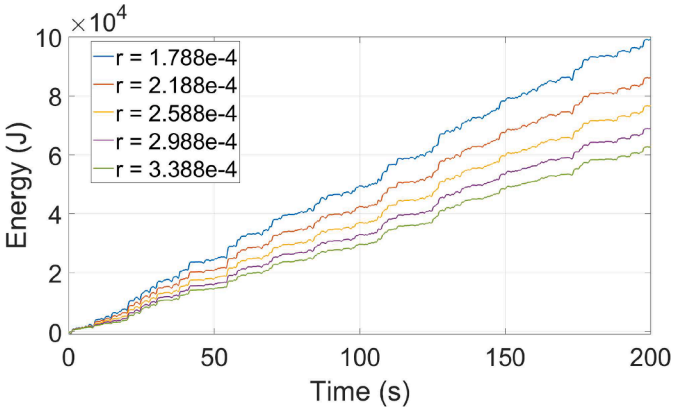

Fig. 7. Energy output comparison using the conventional MPC with different tuning of r.

constraints, and prediction horizon ($T_p = 1.0$ s, corresponding to 10 steps). The only difference is that the EMPC uses predicted future wave excitations, while the conventional MPC uses current and past wave measurements for causal calculations. Both controllers use the same cost function weights and solver configuration to ensure consistency in optimisation conditions.

For both the proposed non-causal EMPC and the conventional MPC, the objective function based on (32) is employed, with the weighting coefficient r designed according to the principle in (39). When $r = 0$, the original cost function becomes non-convex with respect to the optimisation variable c, rendering the problem invalid for convex optimisation methods. Experiments have found that feasibility and constraint satisfaction can only be guaranteed when $r \geq 1.788 \times 10^{-4}$. When $r = 1.787 \times 10^{-4}$, the optimisation problem fails to obtain a feasible solution. When the parameter r approaches a critical value, the optimisation problem exhibits high sensitivity to numerical perturbations, indicating that the condition number of the Hessian matrix in this region increases rapidly and numerical stability decreases. At this point, the margin of positive definiteness weakens, and the solver becomes extremely sensitive to initial values and round-off errors, potentially leading to infeasibility or unstable convergence. With slightly larger values of r, the numerical conditioning of the Hessian gradually improves, and the optimisation problem regains strict convexity and stability. To ensure that the solution remains positive definite and numerically stable over the entire operating range, the following selection criterion is used. Select the smallest r that is practically well-conditioned within the solver's tolerances, such that the optimisation problem remains strictly

Table 5
Energy output comparison table using the conventional MPC with different tuning of r.

r ($\times 10^{-4}$)	3.388	2.988	2.588	2.188	1.788	1.787
Energy (J)	62804.3	69020.2	76702.5	86297.4	99247.3	Infeasible

Table 6
Energy with r under different sea states.

r	Sea state - Energy [kJ]		
	Light	Moderate	Heavy
1.788×10^{-4}	129.64	127.86	121.51
1.988×10^{-4}	127.87	122.47	119.97
2.188×10^{-4}	104.85	101.66	98.73
2.388×10^{-4}	79.11	76.60	74.48
2.588×10^{-4}	55.43	54.29	52.00

convex and numerically stable, and no infeasibility or unstable convergence is observed over the operating range. Applying this criterion yields $r = 1.788 \times 10^{-4}$, which serves as a practical lower bound for the regularisation parameter. This setting effectively avoids pathological behaviour caused by near-singular regions and achieves a good balance between control stability and energy optimisation performance. It is important to note that the simulation precision of 10^{-3} amplifies the sensitivity near the critical value r, resulting in an apparent "jump". This phenomenon is an amplification of numerical pathologies in the critical region at the selected numerical precision, and does not indicate physical model instability or structural instability in the algorithm. Therefore, the apparent discontinuity is primarily a numerical artifact caused by the precision setting, and its root cause remains inherent pathologies in the critical region. The current MPC framework allows for flexible adjustment of the parameter r through experimentation. The relationship between energy output and different r values can be analysed, and then MPC strategies can be compared. Fig. 7 illustrates the energy output of the WEC under the conventional MPC with different values of r, and the corresponding results are summarised in Table 5. The optimal energy output adjustment scheme yields 99.25 kJ at $r = 1.788 \times 10^{-4}$. This value ensures optimisation problem convexity while balancing control performance and computational feasibility, thereby improving the robustness of the optimal solution.

Fig. 5 illustrates the gradual tightening of the control input constraint set $\mathbb{U}_k$, where $k \in \mathbb{I}_{[0,9]}$. As the number of forecast steps increases, the feasible region (horizontal interval) gradually shrinks, reflecting a dynamic tightening characteristic along the forecast horizon. The outer bound $\mathbb{U}_0$ corresponds to the initial moment and allows for greater control freedom. The inner bound $\mathbb{U}_9$ represents the most stringent constraint at the end of the forecast. This tightening mechanism ensures that control inputs remain within a safe range throughout the forecast horizon and remain feasible in the presence of model uncertainties and perturbations. The symmetrical tightening of the constraints around the zero axis indicates consistency in both positive and negative directions.

With the aim of assessing the robustness of the convexification parameter r, the energy-capture metric was evaluated for $r \in \{1.788, 1.988, 2.188, 2.588, 2.788\} \times 10^{-4}$ under three controlled scenarios-sea state, signal-to-noise ratio (SNR), and prediction error within the same EMPC framework (see Tables 6–8). In these tests, the SNR bias is applied to the measured output y_k, and the prediction bias is applied to the predicted wave-excitation amplitude. The results show that, across all scenarios, the row-wise energy decreases monotonically as r increases and the ranking is consistent, indicating that the selected r is robust to variations in sea state, SNR, and prediction error. Based on these results, $r = 1.788 \times 10^{-4}$ is adopted uniformly.

For analysing the impact of prediction horizon length on control performance, this paper conducted prediction horizon sweep experiments under the same EMPC framework, setting the prediction horizons to

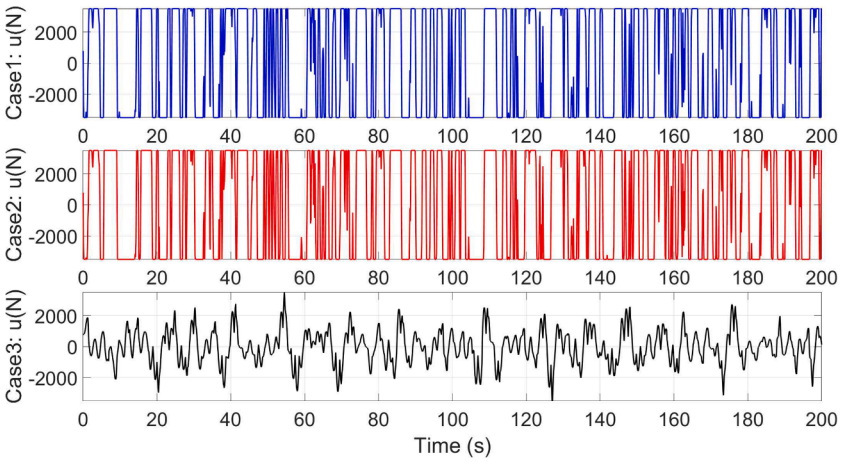

Fig. 8. Control input response comparison. The proposed non-causal EMPC with accurate predictions (blue solid line). The proposed non-causal EMPC with inaccurate predictions (red solid line). The conventional MPC (black solid line).

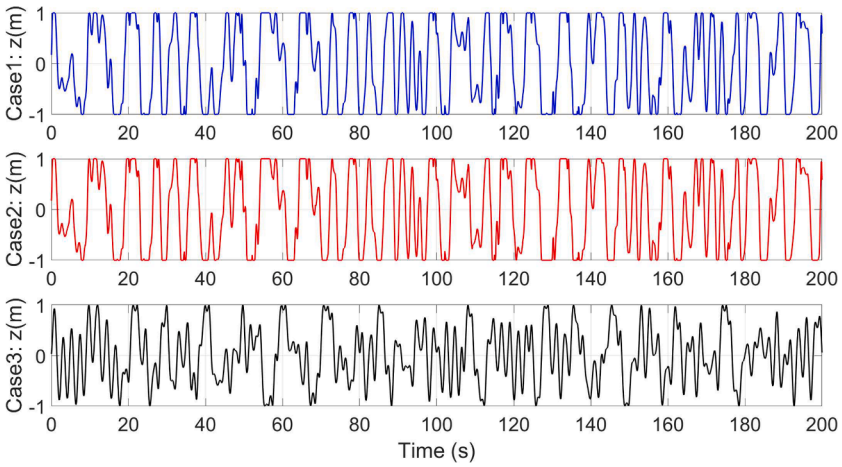

Fig. 9. Heave displacement response comparison. The proposed non-causal EMPC with accurate predictions (blue solid line). The proposed non-causal EMPC with inaccurate predictions (red solid line). The conventional MPC (black solid line).

Table 7
Energy with r under different SNR levels.

r	SNR-Energy [kJ]		
	30 dB	40 dB	50 dB
1.788×10^{-4}	129.02	127.78	127.73
1.988×10^{-4}	124.92	122.98	122.45
2.188×10^{-4}	102.43	101.75	101.61
2.388×10^{-4}	78.48	76.59	76.52
2.588×10^{-4}	56.45	54.53	54.25

Table 8
Energy with r under prediction bias.

r	Prediction bias - Energy [kJ]		
	5 % bias	10 % bias	20 % bias
1.788×10^{-4}	127.77	127.64	127.30
1.988×10^{-4}	122.43	122.38	122.25
2.188×10^{-4}	101.60	101.55	101.44
2.388×10^{-4}	76.58	76.56	76.52
2.588×10^{-4}	54.26	54.24	54.19

$T_p = 0.5$ s, 1.0 s, and 2.0 s. The model parameters, wave input, and controller structure remained consistent across all operating conditions; only the wave prediction horizon varied. Table 9 presents the energy absorption results for different prediction horizons. As the prediction horizon increases from 0.5 s to 2.0 s, the energy decreases slightly and then levels off. While shorter prediction horizons yield slightly higher energy, they also lead to more aggressive control behaviour. Longer prediction horizons, however, suffer from accumulated prediction errors, resulting in limited performance improvements. Considering prediction accuracy, feasibility, and computational cost, this paper adopts $T_p = 1.0$ s as the baseline prediction horizon.

Table 9
Effect of prediction horizon length on energy.

Prediction horizon T_p (s)	Energy (kJ)
0.5	132.53
1.0 (baseline)	127.86
2.0	126.14

For an evaluation of the controller's dependence on prediction accuracy, this paper systematically examines three typical degradation scenarios: constant bias, root mean square error (RMSE), and missing prediction data. The results are shown in Table 10. The proposed non-causal EMPC is highly robust to prediction errors: when the bias and missing data rates increase to 20 %, the energy decreases by less than 0.5 %. When the RMSE increases from 0.741 to 3.048, the energy decreases by only approximately 3.9 %. This demonstrates

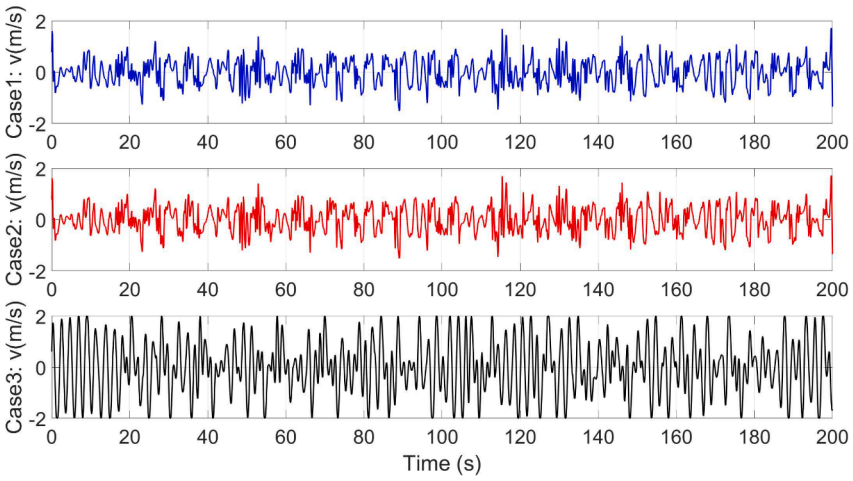

Fig. 10. Heave velocity response comparison. The proposed non-causal EMPC with accurate predictions (blue solid line). The proposed non-causal EMPC with inaccurate predictions (red solid line). The conventional MPC (black solid line).

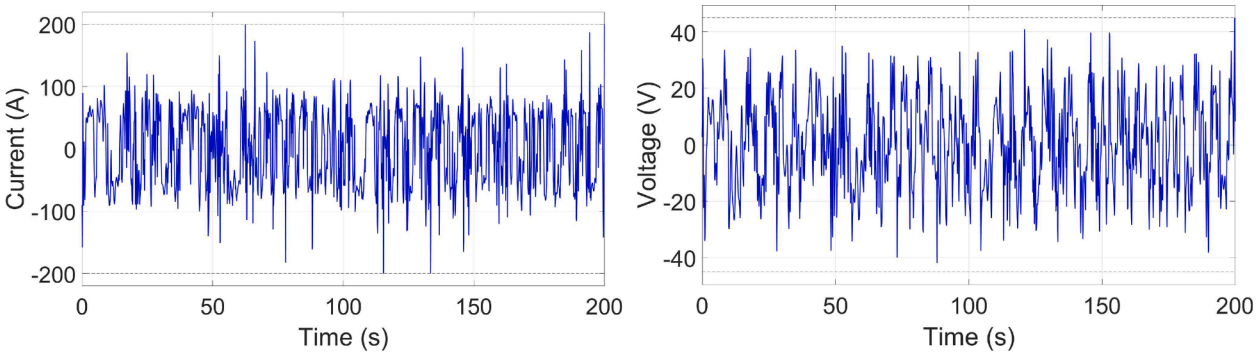

(a) Generator current response. (b) Generator voltage response.

Fig. 11. Generator current and voltage responses.

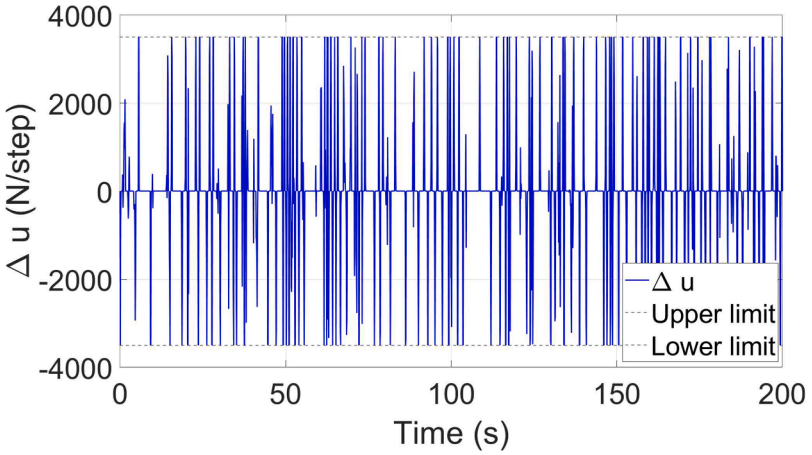

Fig. 12. Control input rate of change (PTO force-rate, Δu).

that the controller can maintain stable and near-optimal performance despite significant degradation in prediction accuracy, validating its practical reliability and engineering feasibility under imperfect wave prediction.

To systematically verify the effectiveness of the proposed non-causal EMPC strategy, this study selected measured wave data from the coast of Cornwall, UK. Based on the acquired raw data, an autoregressive (AR) model was used to construct a wave prediction sequence, which provides feedforward information for the model predictive controller. While preserving the measured wave characteristics, a statistically consistent predicted wave signal was obtained. Fig. 6 shows a comparison of the actual wave excitation force curves calculated from the measured data and the wave excitation force curves generated from the prediction data, visually demonstrating the accuracy and effectiveness of the prediction model in capturing the key wave dynamic characteristics. The comparison results were evaluated using the root mean square error

Table 10
Sensitivity of energy to prediction accuracy (bias, RMSE, and missing data).

Condition	Parameter value	Energy (kJ)
Bias influence		
0 % bias (baseline)	0	127.86
+10 % bias	+0.1	127.64
+20 % bias	+0.2	127.30
RMSE influence		
RMSE = 0.741 (baseline)	0.741	127.86
RMSE = 1.761	1.761	124.97
RMSE = 3.048	3.048	122.85
Missing data influence		
0 % missing (baseline)	0.0	127.86
10 % missing	0.1	127.62
20 % missing	0.2	127.33

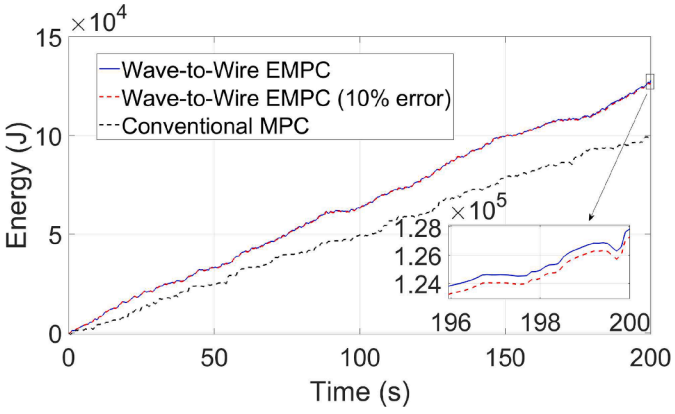

Fig. 13. Energy output comparison. The proposed non-causal EMPC with accurate predictions (blue solid line). The proposed non-causal EMPC with inaccurate predictions (red dashed line). The conventional MPC (black dashed line).

Table 11
Statistical comparison of energy between noncausal EMPC and MPC under five wave series.

Wave series	MPC (kJ)	EMPC (kJ)	fEnergy gain (%)
1	99.25	127.86	+28.8
2	96.61	121.96	+26.2
3	81.12	103.65	+27.8
4	76.93	99.33	+29.1
5	71.23	90.89	+27.6
Average ± SD	85.03 ± 12.3	108.74 ± 15.6	+27.9 ± 1.1

(RMSE), which was 0.741. This confirms the high agreement between the measured and predicted wave forces.

The Figs. 8, 9, and 10 show the time responses of the control input, displacement, and velocity, respectively, generated using the EMPC framework. Both state and control input constraints are satisfied, and the control method has achieved its maximum energy conversion limit. Case 1 shows the proposed non-causal EMPC with accurate wave excitation predictions (blue solid line). Case 2 shows the proposed non-causal EMPC with a prediction error of 10 % (red solid line). Case 3 shows conventional MPC with an optimal parameter of $r = 1.788 \times 10^{-4}$ (black solid line).

Fig. 11(a) and (b) show the generator phase current and terminal voltage during the non-causal EMPC operation, respectively. Both signals remain within safety margins, exhibiting no significant overshoot or distortion. The energy output for the two scenarios is compared in Fig. 13. The energy output of the conventional MPC is 99.25 kJ, while that of the non-causal EMPC is 127.86 kJ, representing a 28.8 % increase

Table 12
Physical parameters of the wave-to-wire model.

Description	Notation	Value
Pole pairs	p	43
Effective radius	r_{eq}	0.45 m
Permanent magnet flux	ψ_f	0.28 Wb
Stator resistance	R_s	0.2 Ω
d-axis inductance	L_d	0.02 H
q-axis inductance	L_q	0.02 H
Maximum q-axis current	$i_{q,\max}$	200 A
Maximum q-axis voltage	$v_{q,\max}$	45 V
q-axis PI gains	$(K_{p,q}, K_{i,q})$	(0.06, 0.6)
d-axis PI gains	$(K_{p,d}, K_{i,d})$	(0.06, 0.6)

in energy output. Since the conventional MPC adopts the same finite-horizon QP structure as commercialised MPC controllers, it serves as a realistic industrial baseline for evaluating control performance. This is due in part to the fact that the state and input trajectories using the non-causal EMPC, shown in Figs. 8 and 9, are closer to the boundaries in most cases compared to the conventional MPC. This means that the limits of the WEC design and the PTO mechanism are more effectively utilised. In addition to amplitude bound on the PTO force, the discrete rate constraint (12) is enforced. Fig. 12 shows the time profile of the control increment $\Delta u_k := u_k - u_{k-1}$. All samples satisfy $|\Delta u_k| \le \dot{u}_{\max} T_s$ over the whole window, and no violations occur. This confirms closed-loop compliance with the rate constraint.

The consistency of control performance was evaluated using five independent wave sequences with statistically equivalent spectra. As summarised in Table 11, the average energy of the proposed non-causal EMPC is 108.74 Â± 15.6 kJ, an improvement of approximately +27.9 Â± 1.1 % over the baseline MPC (85.03 Â± 12.3 kJ). The low variance indicates that the energy enhancement is statistically stable, confirming the robustness and general applicability of the proposed control strategy.

5. Conclusions

This paper proposes a non-causal economic model predictive control (EMPC) based on a wave-to-wire model for the control of wave energy converters (WECs), taking into account the computational limitations of embedded systems. Wave prediction is implemented using an autoregressive model, and parameter identification is performed via recursive least squares (RLS). Under the estimated wave state, the controller operates in a 5-second training and 1-second prediction cycle, using piecewise prediction to reduce computational overhead. The wave-to-wire model is integrated within the same optimisation framework. During optimisation, hard constraints tied to electrical limits are imposed on the PTO force-rate, ensuring electrical feasibility is enforced at every step. This approach unifies economic objectives, the wave-to-wire model, and engineering feasibility into a single optimisation problem.

Simulation results demonstrate that, compared with traditional control methods, the proposed non-causal EMPC approach significantly improves the WEC's energy conversion efficiency while maintaining safe operation under varying sea conditions. By incorporating a hard constraint on the PTO force-rate into the optimisation, the mechanical-economic objective is tightly coupled with electrical feasibility, reducing the risk of infeasible commands and suppressing potential instability. Current, voltage, and PTO force-rate are maintained within predefined limits. This framework concurrently verifies constraint satisfaction and energy metrics within the same control loop, ensuring feasibility for real-time deployment. Key properties such as recursive feasibility and robust constraint satisfaction are demonstrated. The non-causal EMPC demonstrates robust performance even in the presence of reasonable prediction errors. The introduction of the autoregressive model further enhances the system's environmental adaptability and control accuracy.

Overall, this research aims to implement real-time non-causal EMPC on a platform with limited computational resources, providing new possibilities for intelligent control applications in harsh marine environments. However, this method still relies on prediction accuracy, and large errors may affect economic optimisation results. Furthermore, current validation is primarily based on idealised numerical models, which do not fully consider complex sea conditions and equipment nonlinearities.

Future work will focus on extending non-causal EMPC to nonlinear systems and introducing more advanced wave prediction methods to further improve prediction accuracy. The stability and robustness of this method will be verified under more complex and variable real-world sea conditions, and hardware-in-the-loop (HIL) simulations will be conducted to evaluate its real-time performance and feasibility in actual engineering environments. Current/voltage peaks and constraint switching will be quantified under different sea states and longer timescales. The impact of the PTO force-rate hard constraint on the energy-feasibility trade-off will be analysed, and robustness bounds will be defined across a wider range of operating conditions.

Furthermore, future research will explore the integration of non-causal EMPC with various renewable energy sources, and conduct long-term reliability evaluations to demonstrate the stability and effectiveness of such systems under real-world operating conditions.

CRediT authorship contribution statement

Teng Gao: Writing – review & editing, Writing – original draft, Visualization, Validation, Software, Methodology, Investigation, Formal analysis, Data curation, Conceptualization; **Yao Zhang:** Writing – review & editing, Supervision, Resources, Project administration, Funding acquisition, Conceptualization; **Tahsin Tezdogan:** Writing – review & editing, Supervision.

Declaration of competing interest

The authors declare that they have no competing financial interests or personal relationships that could have appeared to influence the work reported in this manuscript.

Acknowledgments

This work was funded by the Wave Energy Scotland Direct Generation Competition, the UK Royal Society IEC-NSFC (223485), and the Innovate UK GREENPORTSIDE project.

References

Amundarain, M., Alberdi, M., Garrido, A.J., Garrido, I., 2010. Modeling and simulation of wave energy generation plants: output power control. IEEE Trans. Ind. Electron. 58 (1), 105–117.

Atyabi, A., Shic, F., Naples, A., 2016. Mixture of autoregressive modeling orders and its implication on single trial EEG classification. Expert Syst. Appl. 65, 164–180.

Drew, B., Plummer, A., Sahinkaya, M., 2009. A review of wave energy converter technology. Proc. Inst. Mech. Eng. Part A J. Power Energy 223 (8), 887–902. https://doi.org/10.1243/09576509JPE782

Eriksson, S., 2019. Design of permanent-magnet linear generators with constant-torque-angle control for wave power. Energies 12 (7), 1312.

Evans, M.A., Cannon, M., Kouvaritakis, B., 2014. Robust MPC tower damping for variable speed wind turbines. IEEE Trans. Contr. Syst. Technol. 23 (1), 290–296.

Falnes, J., Kurniawan, A., 2020. Ocean Waves and Oscillating Systems: Linear Interactions Including Wave-Energy Extraction. Vol. 8. Cambridge university press.

Gao, T., Zhang, Y., Tezdogan, T., 2025. Noncausal explicit model predictive control of wave energy converters. Ocean Eng. 338, 121999.

García-Violini, D., Faedo, N., Peña-Sanchez, Y., Nava, V., Ringwood, J.V., 2024. Revisiting excitation force estimation in WECs: on the (mis) use of structure-based estimation approaches. Ocean Eng. 311, 118864.

Garcia-Violini, D., Ringwood, J.V., 2021. Energy maximising robust control for spectral and pseudospectral methods with application to wave energy systems. Int. J. Contr. 94 (4), 1102–1113.

Gunn, K., Stock-Williams, C., 2012. Quantifying the global wave power resource. Renew. Energy 44, 296–304.

Hals, J., Falnes, J., Moan, T., 2011. A comparison of selected strategies for adaptive control of wave energy converters. J. Offshore Mech. Arct. Eng. 133 (3), 031101. https://doi.org/10.1115/1.4002735

Igic, P., Zhou, Z., Knapp, W., MacEnri, J., Sørensen, H.C., Friis-Madsen, E., 2011. Multi-megawatt offshore wave energy converters–electrical system configuration and generator control strategy. IET Renewable Power Gener. 5 (1), 10–17.

Josset, C., Babarit, A., Clément, A.H., 2007. A wave-to-wire model of the SEAREV wave energy converter. Proc. Inst. Mech. Eng. Part M J. Eng. Marit. Environ. 221 (2), 81–93.

Kolmanovsky, I., Gilbert, E.G., 1995. Maximal output admissible sets for discrete-time systems with disturbance inputs. In: Proceedings of 1995 American Control Conference-ACC'95. Vol. 3. IEEE.

Lasheen, A., Saad, M.S., Emara, H.M., Elshafei, A.L., 2017. Continuous-time tube-based explicit model predictive control for collective pitching of wind turbines. Energy 118, 1222–1233.

Li, G., Belmont, M.R., 2014. Model predictive control of sea wave energy converters–part i: a convex approach for the case of a single device. Renew. Energy 69, 453–463.

Manan Jariwala, A., Kumar Dash, S., Sahu, U.K., Mohan, H.M., 2025. Performance optimization techniques on point absorber and oscillating water column wave energy converter: a comprehensive review. IEEE Access 13, 14743–14759. https://doi.org/10.1109/ACCESS.2025.3531298

Mayne, D.Q., Raković, S.V., Findeisen, R., Allgöwer, F., 2006. Robust output feedback model predictive control of constrained linear systems. Automatica 42 (7), 1217–1222.

Müller, M.A., Grüne, L., 2016. Economic model predictive control without terminal constraints for optimal periodic behavior. Automatica 70, 128–139.

Murai, M., Li, Q., Funada, J., 2021. Study on power generation of single point absorber wave energy converters (PA-WECs) and arrays of PA-WECs. Renew. Energy 164, 1121–1132.

Penalba, M., Ringwood, J.V., 2016. A review of wave-to-wire models for wave energy converters. Energies 9 (7), 506.

Salter, S.H., 1974. Wave power. Nature 249 (5459), 720–724.

Schiavon, R., Vanzan, D., Zampato, M., Alessi, A., Bonfanti, M., Bracco, G., Capello, E., 2021. An application of the tube_based robust model predictive control to optimize energy extraction on a inertial sea wave energy converter. In: Offshore Mediterranean Conference and Exhibition. OMC, pp. OMC–2021.

Weiss, G., Li, G., Mueller, M., Townley, S., Belmont, M.R., 2012. Optimal control of wave energy converters using deterministic sea wave prediction. In: The Energy & Materials Research Conference, Torremolinos, Malaga, Spain.

Wijaya, V.V., Zhang, Y., Edwards, C., Li, G., Belmont, M., 2025. Sliding mode observer based non-causal model predictive control for collision-free marine launch and recovery system. Ocean Eng. 340, 122354.

Wilson, D.G., Weaver, W.W., Robinett, R.D., Glover, S.F., 2018. Nonlinear power flow control design for networked AC/DC based microgrid systems. In: 2018 Annual American Control Conference (ACC). IEEE, pp. 5698–5705.

Zhan, S., Li, G., Bailey, C., 2019a. Economic feedback model predictive control of wave energy converters. IEEE Trans. Ind. Electron. 67 (5), 3932–3943.

Zhan, S., Li, G., Na, J., He, W., 2019b. Feedback noncausal model predictive control of wave energy converters. Contr. Eng. Pract. 85, 110–120.

Zhang, M., Yu, S.-R., Zhao, G.-W., Dai, S.-S., He, F., Yuan, Z.-M., 2024a. Model predictive control of wave energy converters. Ocean Eng. 301, 117430.

Zhang, Y., Edwards, C., Belmont, M., Li, G., 2023. Robust model predictive control for constrained linear system based on a sliding mode disturbance observer. Automatica 154, 111101.

Zhang, Y., Li, G., 2019. Non-causal linear optimal control of wave energy converters with enhanced robustness by sliding mode control. IEEE Trans. Sustainable Energy 11 (4), 2201–2209.

Zhang, Y., Li, G., 2022. Robust tube-based model predictive control for wave energy converters. IEEE Trans. Sustainable Energy 14 (1), 65–74.

Zhang, Y., Li, G., Al-Ani, M., 2024b. Robust learning-based model predictive control for wave energy converters. IEEE Trans. Sustainable Energy 15 (3), 1957–1967.

Zhang, Y., Zeng, T., Li, G., 2019. Robust excitation force estimation and prediction for wave energy converter m4 based on adaptive sliding-mode observer. IEEE Trans. Ind. Inf. 16 (2), 1163–1171.

Zhang, Y., Zhan, S., Li, G., 2020. Model predictive control of wave energy converters with prediction error tolerance. IFAC-PapersOnLine 53 (2), 12289–12294.